Quantifying the Dzyaloshinskii-Moriya Interaction Induced by the Bulk Magnetic Asymmetry

Qihan Zhang,[1,2,*] Jinghua Liang,[3,*] Kaiqi Bi,[4,*] Le Zhao,[1,2] He Bai,[5] Qirui Cui,[3]
Heng-An Zhou,[1,2] Hao Bai,[1,2] Hongmei Feng,[1,2] Wenjie Song,[6] Guozhi Chai,[6] O. Gladii,[7]
H. Schultheiss,[7] Tao Zhu,[5,8] Junwei Zhang,[4] Yong Peng,[4,†] Hongxin Yang,[3,9,‡] and Wanjun Jiang[1,2,§]

[1]State Key Laboratory of Low-Dimensional Quantum Physics and Department of Physics, Tsinghua University,
Beijing 100084, China
[2]Frontier Science Center for Quantum Information, Tsinghua University, Beijing 100084, China
[3]Ningbo Institute of Materials Technology and Engineering, Chinese Academy of Sciences, Ningbo 315201, China
[4]School of Materials and Energy, Electron Microscopy Centre of Lanzhou University, Lanzhou University,
Lanzhou 730000, China
[5]Spallation Neutron Source Science Center, Dongguan 523803, China
[6]Key Laboratory of Magnetism and Magnetic Materials of Ministry of Education, Lanzhou University, Lanzhou 730000, China
[7]Institut für Ionenstrahlphysik und Materialforschung, Helmholtz-Zentrum Dresden-Rossendorf, D-01328 Dresden, Germany
[8]Beijing National Laboratory for Condensed Matter Physics and Institute of Physics, Chinese Academy of Sciences,
Beijing 100190, China
[9]Center of Materials Science and Optoelectronics Engineering, University of Chinese Academy of Sciences,
Beijing 100049, China

A broken interfacial inversion symmetry in ultrathin ferromagnet/heavy metal (FM/HM) bilayers is generally believed to be a prerequisite for accommodating the Dzyaloshinskii-Moriya interaction (DMI) and for stabilizing chiral spin textures. In these bilayers, the strength of the DMI decays as the thickness of the FM layer increases and vanishes around a few nanometers. In the present study, through synthesizing relatively thick films of compositions CoPt or FePt, CoCu or FeCu, FeGd and FeNi, contributions to DMI from the composition gradient-induced bulk magnetic asymmetry (BMA) and spin-orbit coupling (SOC) are systematically examined. Using Brillouin light scattering spectroscopy, both the sign and amplitude of DMI in films with controllable direction and strength of BMA, in the presence and absence of SOC, are experimentally studied. In particular, we show that a sizable amplitude of DMI (± 0.15 mJ/m^2) can be realized in CoPt or FePt films with BMA and strong SOC, whereas negligible DMI strengths are observed in other thick films with BMA but without significant SOC. The pivotal roles of BMA and SOC are further examined based on the three-site Fert-Lévy model and first-principles calculations. It is expected that our findings may help to further understand the origin of chiral magnetism and to design novel noncollinear spin textures.

Introduction.—In ultrathin ferromagnet/heavy metal (FM/HM) bilayers, an interfacial asymmetry combined with a strong spin-orbit coupling (SOC) establishes an interfacial Dzyaloshinskii-Moriya interaction (DMI) that gives rise to exciting spin-orbitronic physics [1–6]. Some examples are the observation of chiral domain walls [7–11], Néel skyrmions [12–16], and the driven motion of magnetic domains and skyrmions by spin torques [7,9,13,15,17,18]. The SOC strength is not a readily adjustable material parameter, but symmetry breaking can be introduced by different means [19–24]. For example, early work in GdFeCo amorphous films revealed how a naturally existing composition gradient along the thickness direction introduces a bulk DMI [20]. However, a clear mechanistic explanation and, more importantly,

successful control of both the sign and amplitude of DMI induced by the composition gradient-induced bulk magnetic asymmetry (BMA) are not established. Note that BMA in Fe$_{1-x}$Pt$_x$ films could lead to bulk spin torques, which result in a self-switching [23,25–27].

Based on the three-site Fert-Lévy model [28–30], the occurrence of DMI between neighboring magnetic atoms (sites i and j) is enabled by the SOC of the HM atom (site l) via conduction electrons. The resultant DM vector D_{ijl} reads as [28]

$$\vec{D}_{ijl}(\vec{R}_{li}, \vec{R}_{lj}, \vec{R}_{ij}) = -V_1 \frac{(\vec{R}_{li} \cdot \vec{R}_{lj})(\vec{R}_{li} \times \vec{R}_{lj})}{|\vec{R}_{li}|^3 |\vec{R}_{lj}|^3 |\vec{R}_{ij}|}, \quad (1)$$
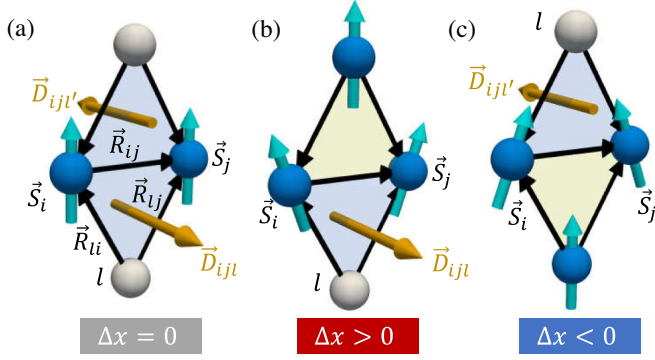
FIG. 1. The schematic diagram of the three-site Fert-Lévy model. (a) The schematic illustration of the atom and spin structures without BMA; the DM vectors $\vec{D}_{ijl}$ and $\vec{D}_{ijl'}$ are described by the three-site Fert-Lévy model. The blue (gray) balls represent the FM and HM atoms. $\vec{R}_{li}$ and $\vec{R}_{lj}$ are the intersite vectors. (b),(c) The asymmetric spin structure for systems with opposite BMA ($\pm\Delta x$) exhibit nonzero opposite DMI vectors.

where $\vec{R}_{li}$, $\vec{R}_{lj}$, and $\vec{R}_{ij}$ are the corresponding distance vectors and V_1 is a SOC-governed material parameter. For thick films without BMA, DM vectors ($\vec{D}_{ijl}$ and $\vec{D}_{ijl'}$) on the opposite sides of the FM atoms are compensated, as shown in Fig. 1(a). In the presence of BMA, finite, uncompensated DM vectors can be found, as shown in Figs. 1(b) and 1(c), respectively. In particular, the sign of the uncompensated DM vector is determined by the direction of BMA. In the present work, the role of both BMA and SOC for producing DMI will be experimentally examined.

Synthesis of thick films with bulk magnetic asymmetry.— The presence of BMA is introduced by varying the relative composition of binary alloys (FM_xNM_{1-x}) along with the thickness (t) direction, where FM denotes the magnetic element (Co and Fe) and NM is the nonmagnetic metal with (or without) SOC. We define the starting (x_i) and ending (x_t) compositions as $FM_{x_{i,t}}NM_{1-x_{i,t}}$. The composition gradient reads as $\Delta x/t = (x_t - x_i)/t$, where $\Delta x = x_t - x_i$ is the composition difference between the ending and starting layers. The corresponding magnetization gradient reads as $\Delta M_s/t = (M_s^t - M_s^i)/t$, where $M_S^{i,t}$ are the saturation magnetization of the starting and ending layers, respectively.

Binary magnetic films with in-plane magnetic anisotropy are grown using the cosputtering technique. During the growth, the relative deposition rates of the FM and NM elements are linearly changed, which create a linear composition-magnetization difference along the growth direction. Multilayers of stacking order Ta(3 mm)/ FM_xNM_{1-x}(t mm)/Ta(3 mm) are synthesized, in which the choice of both FM/NM elements, the direction of composition difference ($\pm\Delta x$), the effect of magnetization differences ($\Delta M_s/\Delta x$), and the thickness (t) will be studied. A full list of samples together with the key parameters are listed in Table S1 in part S2 of Supplemental Material [31].

The presence of composition differences is examined by using a high-angle annular dark-field scanning transmission electron microscopy (HAADF-STEM). HAADF-STEM images obtained from two representative samples, CoPt ($\Delta x = \pm 52\%$), are shown in Figs. 2(a) and 2(e). The opposite contrast changes within the images are associated with the opposite composition differences, which are further verified using energy-dispersive x-ray spectroscopy (EDS), as shown in Figs. 2(b) and 2(f), respectively. The
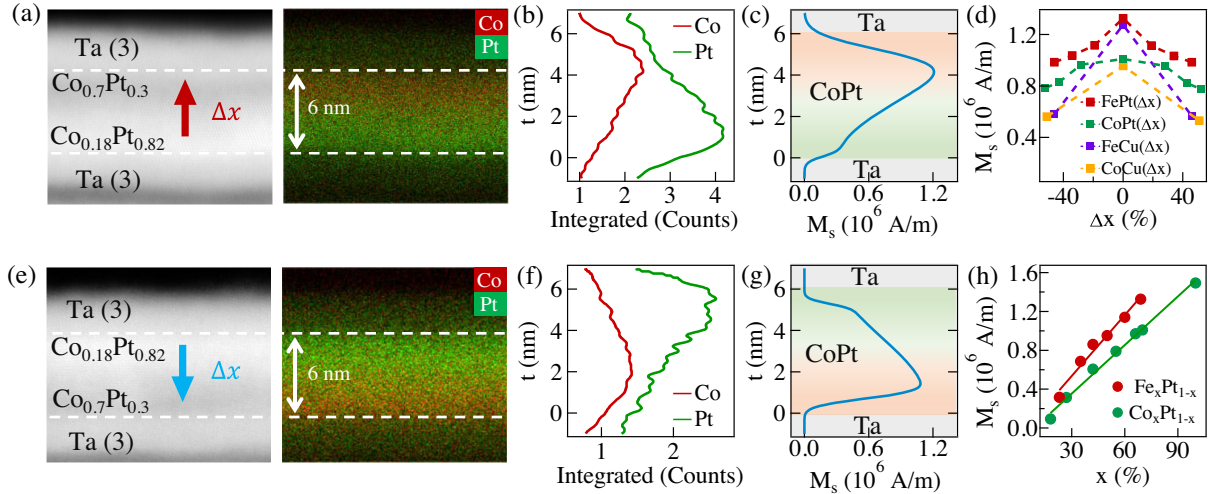
FIG. 2. Structural and magnetic evidence of BMA in CoPt ($\Delta x = \pm 52\%$). The HAADF-STEM images of films with $\Delta x = +52\%$ (a) and $\Delta x = -52\%$ (e), respectively. For the $\Delta x = +52\%$ ($\Delta x = -52\%$), compositions from bottom to top change from $Co_{0.18}Pt_{0.82}$ ($Co_{0.7}Pt_{0.3}$) to $Co_{0.7}Pt_{0.3}$ ($Co_{0.18}Pt_{0.82}$), respectively. The opposite trends of contrast reveal an opposite element distribution of Co/Pt (red/green). (b),(f) The EDS line profiles. (c),(g) The magnetization depth profiles from the PNR measurement. (d) The dependence of M_s vs Δx in CoPt (Δx), FePt (Δx), CoCu (Δx), and FeCu (Δx) films. (h) The evolution of M_s vs x in films without gradient ($\Delta x = 0$).

composition gradients are also studied in other films (see part S5 of Supplemental Material [31]).

To correlate the composition and magnetization gradients, we conducted polarized neutron reflectometry (PNR) measurement (see Supplemental Material [31]). From the nuclear scattering length density, opposite trends of composition from $Co_{0.25}Pt_{0.75}$ to $Co_{0.63}Pt_{0.37}$ (for $\Delta x = +52\%$) and from $Co_{0.63}Pt_{0.37}$ to $Co_{0.25}Pt_{0.75}$ (for $\Delta x = -52\%$) are revealed. Based on the profile of magnetic scattering length density, the corresponding magnetization gradients are further estimated, as shown in Figs. 2(c) and 2(g), respectively. From the PNR measurement, values of M_s for $Co_{0.25}Pt_{0.75}$ and $Co_{0.63}Pt_{0.37}$ are determined to be 0.453×10^6 and 1.082×10^6 A/m, respectively. By using a quasilinear approximation, the ratio of $\Delta M_s / \Delta x = 1.655 \times 10^6$ A/m is determined.

A monotonic decrease of M_s, following the increase of Δx, is measured by vibrating sample magnetometry, as shown in Fig. 2(d). For samples with opposite composition gradients ($\pm \Delta x$), values of M_s remain approximately the same. For films with homogenous compositions ($\Delta x = 0$), a linear dependence of M_s as a function of homogenous composition (x) is obtained for Co_xPt_{1-x} and Fe_xPt_{1-x} films, as shown in Fig. 2(h). The linear slope of $M_s(x)$ is calculated, which enables the ratio of $\Delta M_s / \Delta x$ (in the unit of 10^6 A/m) to be obtained: 1.67 for CoPt (Δx), 2.09 for FePt (Δx), 1.31 for CoCu (Δx), and 1.78 for FeCu (Δx), respectively. These values are in agreement with the PNR results. Upon establishing a quasilinear relation of $\Delta M_s / \Delta x$, we use Δx to represent the magnetization gradient ($\Delta M_s / t$, with $t = 6$ nm).

Measurement of the strength of DMI induced by BMA.— By using Brillouin light scattering (BLS) spectroscopy, both the amplitude and sign of DMI can be determined through measuring the nonreciprocal frequency shift of Damon-Eshbach (DE) spin waves [44–48], as schematically illustrated in Fig. 3(a). The dispersion of the DE spin waves reads as [48,49]

$$f(\boldsymbol{k}) = \frac{\gamma}{2\pi} \sqrt{(H + J\boldsymbol{k}^2)(H + J\boldsymbol{k}^2 + \mu_0 M_{\mathrm{eff}})} - \mathrm{sgn}(M_z)\frac{\gamma}{\pi M_s}Dk_x, \quad (2)$$

where $J = 2A/M_s$, with A being the exchange constant, D the volume-averaged DMI constant, γ the gyromagnetic ratio, and $\mu_0 M_{\mathrm{eff}}$ the effective demagnetization field. The projection of the spin-wave vector ($\boldsymbol{k}$) in the x direction $k_x = (4\pi/\lambda)\sin\theta$ is determined by the incident angle (θ) and wavelength of the laser ($\lambda = 532$ nm). The frequency shift (Δf) between the counterpropagating spin waves ($\pm k_x$) induced by DMI is given by

$$\Delta f = f_{\mathrm{DM}}(-k_x, M_z) - f_{\mathrm{DM}}(k_x, M_z) = \frac{2\gamma}{\pi M_s}Dk_x. \quad (3)$$

Thus, Δf between the Stokes and anti-Stokes peaks measured at negative and positive fields enables D to be quantified, through a linear fitting of Δf vs k_x.

Typical BLS spectra for CoPt ($\Delta x = \pm 52\%$), with $k_x = 11.8$ rad/μm, are shown in Figs. 3(b) and 3(c).
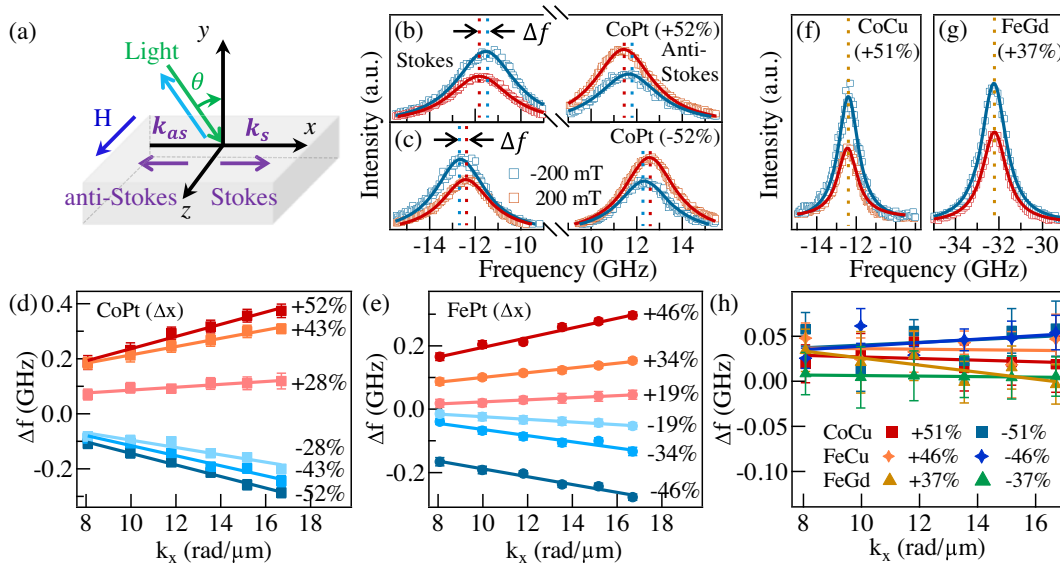
FIG. 3. The frequency shift of the nonreciprocal spin-wave propagation. (a) The setup geometry of the BLS spectroscopy. The anti-Stokes (Stokes) processes correspond to annihilation (creation) of magnons. (b),(c) The BLS spectra for CoPt ($\Delta x = \pm 52\%$) films in which the red (blue) curve represents the spectra with $\pm \mu_0 H$, respectively. (d),(e) The summarized Δf vs k_x for the CoPt ($\pm \Delta x$) and FePt ($\pm \Delta x$) films. (f),(g) The BLS spectra for CoCu ($\Delta x = +51\%$) and FeGd ($\Delta x = +37\%$). (h) The evolution of Δf vs k_x for the CoCu ($\pm \Delta x$), FeCu ($\pm \Delta x$), and FeGd ($\pm \Delta x$) films.

In CoPt ($\Delta x = +52\%$) film, one observes a positive frequency shift ($+\Delta f$) under opposite magnetic fields ($\mu_0 H = \pm 200$ mT), as shown in Fig. 3(b). In CoPt ($\Delta x = -52\%$) film, there, however, exhibits a negative frequency shift ($-\Delta f$), as shown in Fig. 3(c). These opposite frequency shifts ($\pm \Delta f$) imply an opposite sign of DMI in samples with opposite magnetization gradients ($\pm \Delta x$), as suggested by Eq. (3). Figures 3(d) and 3(e) summarize the evolution of Δf vs k_x for CoPt and FePt films, respectively. Following the increase of Δx, the slope of Δf vs k_x increases monotonically. Upon inverting the sign of $\pm \Delta x$, the reversed signs of the slopes suggest that the sign of DMI is related to the direction of BMA. Note that a precise determination of the volume-averaged DMI constant D will be discussed later. A small offset of Δf at $k_x = 0$ from the origin is observed, which may arise from the different magnetic properties of the top and bottom surfaces that naturally lead to an additional asymmetry of the counterpropagating (dipolar) spin waves [50].

To elucidate the necessity of SOC and BMA in producing DMI, three types of reference samples are examined. The first set of samples is Fe_xPt_{1-x} and Co_xPt_{1-x} films with homogeneous compositions (x). These samples contain HMs (and have significant SOC) but have no magnetization gradients and, hence, no BMA ($\Delta x = 0$). The second set of samples is CoCu (Δx), FeCu (Δx), and FeNi (Δx) films. These samples have magnetization gradients ($\Delta x \neq 0$) but no HMs (and have insignificant SOC). The third set of samples is FeGd (Δx) films to clarify whether the SOC from the $4f$ rare-earth metal can also establish a bulk DMI, in the presence of BMA.

In the first type of films ($\Delta x = 0$, $t = 6$ nm), we observe a nearly zero slope from Δf vs k_x, indicating a negligible DMI (see part S6 of Supplemental Material [31]). This observation can be explained by the compensated DMI vectors from the equivalent probability of Pt atoms that appear at the nearest Co/Fe sites, as implied by Fig. 1(a). In the other two sets of samples, the role of SOC is examined via replacing Pt with Cu which exhibits a negligible SOC or with $4f$ rare-earth metal Gd. The BLS spectra of CoCu ($\Delta x = +51\%$) film at $k_x = 11.8$ rad/μm and under $\mu_0 H = \pm 200$ mT are shown in Fig. 3(f), in which the absence of frequency shift is observed. A negligible frequency shift (Δf) is also observed in FeGd ($\Delta x = +37\%$) films at $k_x = 16.7$ rad/μm and under $\mu_0 H = \pm 1000$ mT, as shown in Fig. 3(g). This result indicates that the SOC of the Gd cannot establish a bulk DMI in the FeGd binary films with in-plane anisotropy. The intriguing origin of the bulk DMI observed in GdFeCo and similar compounds [20] may require a revisit. Through identifying a nearly zero slope of Δf vs k_x, vanishingly small DMI values are summarized in Fig. 3(h). Note that a vanishingly small DMI in FeNi ($\Delta x = \pm 48\%$) films is also obtained (see part S6 of Supplemental Material [31]). These experiments suggest
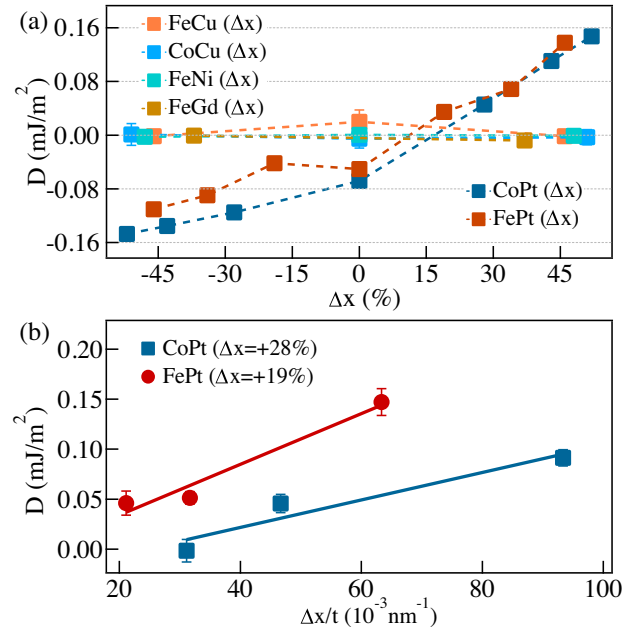
FIG. 4. The experimental results for the DMI induced by the BMA. (a) The volume-averaged DMI constant D for films with varied amplitudes and signs of Δx ($t = 6$ nm). (b) The evolution of D vs $\Delta x/t$ for the CoPt ($\Delta x = +28\%$) and FePt ($\Delta x = +19\%$) films with different thicknesses. The solid line is a linear fitting curve.

that both BMA and SOC from $5d$ HM are corequisites for producing sizable DMI in thick films, as suggested by the Fert-Lévy model.

Summarized in Fig. 4(a) are the volume-averaged DMI constants D. For CoPt (Δx) and FePt (Δx) films, the strength of DMI increases with the increase of the magnetization gradient (Δx), and the polarity of DMI flips upon inverting $\pm \Delta x$. For CoCu (Δx), FeCu (Δx), FeGd (Δx), and FeNi (Δx) films, negligible DMI constants are consistent with the absence of SOC from $5d$ HM. These results further confirm that the nonreciprocity of spin waves originating from dipolar fields [51], interface anisotropies [52], and different values of M_s between the top and bottom magnetic layers are not contributing factors. Note that several $SiN(5 \text{ nm})/FM_xNM_{1-x}(t \text{ nm})/SiN(5 \text{ nm})$ films are also made, in which the same sign and approximately same amplitude of DMI are observed, as shown in Fig. 13 in Supplemental Materials [31]. This result is expected from the negligible (compensated) DMI from the dual interfaces in the $Ta/FM_xNM_{1-x}/Ta$ trilayer.

By fixing the composition of the starting and ending layers [CoPt ($\Delta x = +28\%$) and FePt ($\Delta x = +19\%$)], the BMA-induced DMI is further examined through varying the thickness from 3 to 9 nm. In this case, the values of $M_s^{i,t}$ of the starting and ending layers are fixed. In particular, the linear evolution of D vs $\Delta x/t$ can be found in Fig. 4(b), confirming the key role of BMA in determining the strength of DMI.
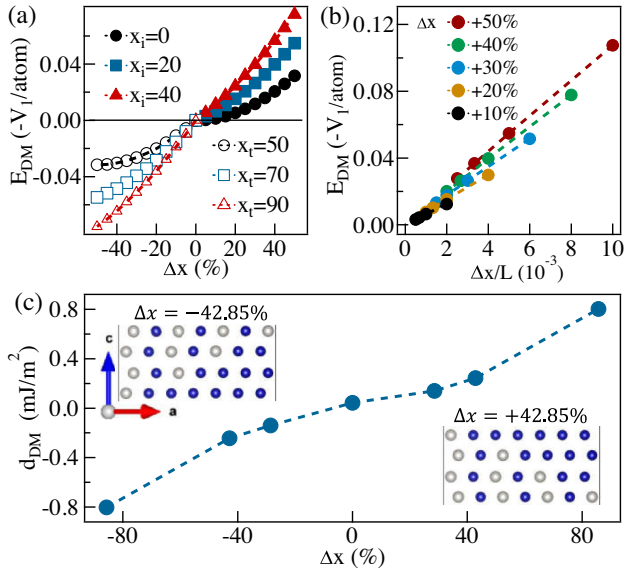
FIG. 5. The calculated DMI induced by the BMA. (a) The calculated DMI energy E_{DM} vs Δx with fixed starting and ending compositions ($x_{i,t}$). (b) The evolution of E_{DM} vs $\Delta x/L$. (c) The first-principles result of the gradient-dependent DMI constants (d_{DM}).

The theoretical formalism of the BMA-induced DMI.—Based on the three-site Fert-Lévy model and the first-principles calculations, the BMA-induced DMI is theoretically examined. Specifically, the total DMI energy (E_{DM}) can be written as [40]

$$E_{DM} = \sum_{i,j,l} \vec{D}_{ijl} \cdot (\vec{S}_i \times \vec{S}_j). \qquad (4)$$

For different starting compositions x_i, with the number of layers $L = 100$, the calculated E_{DM} vs Δx in the framework of the three-site Fert-Lévy model is shown in Fig. 5(a). A monotonical increase of E_{DM} vs Δx, together with a reversed sign of E_{DM} by flipping $\pm\Delta x$ can be observed. In particular, E_{DM} vanishes at $\Delta x = 0$ (without a composition gradient). Upon fixing the composition of the starting and ending layers, the evolution of DMI strength as a function of thickness is also calculated and shown in Fig. 5(b). There, one can find that the calculated E_{DM} monotonically increases with the increased gradient ($\Delta x/L$) under fixed composition differences ($\Delta x = +10\%, +20\%, +30\%, +40\%$, and $+50\%$). This is consistent with our experimental observations shown in Fig. 4(b).

To quantify the strength of BMA-induced DMI, first-principles calculations are also performed (see Supplemental Material [31]). We consider an hcp stacking with lattice parameters being a and $c = 1.6a$, which consists of $100 \times 100 \times 0.5L$ hexagonal unit cells, and calculate the E_{DM} of a cycloidal spin spiral with a small spiral vector $q = (2\pi/100a, 0, 0)$. For example, the

structural configurations with $\Delta x = \pm 42.85\%$ are shown in the insets in Fig. 5(c). The calculated DMI constants (d_{DM}) of the four-layer CoPt thin films with different Δx are shown in Fig. 5(c) in which a nonvanishing DMI for all $\Delta x \neq 0$ films can be identified. Both the sign and magnitude of DMI match with the experimental results [as shown in Fig. 4(a)]. These observations demonstrate that the strength of DMI is directly determined by the amplitude of the magnetization gradient (Δx), the polarity of which is determined by the sign of $\pm\Delta x$.

Conclusions.—The volume-averaged DMI is comprehensively investigated through BLS spectroscopy in CoPt or FePt, CoCu or FeCu, NiFe and FeGd magnetic films with magnetization and composition gradients (Δx) along the growth direction. Through measuring the amplitude and sign of DMI, a connection between the sign (amplitude) of magnetization (composition) gradients ($\pm\Delta x$) and the strong SOC is obtained. In particular, a relatively large DMI value, ± 0.15 mJ/m^2, is obtained in 6-nm-thick CoPt films with $\Delta x = \pm 52\%$, whereas the absence of DMI in other films without involving BMA and SOC is revealed. The evolution of the BMA-induced DMI is theoretically examined through performing atomic calculations, which agrees with the experimental observations. The identification of the bulk DMI that is jointly produced by BMA and SOC of the 5d HM could serve as an important ingredient for the current understandings of chiral magnetism and could help to design novel chiral noncollinear spin textures [53].

*These authors contributed equally to this work.
†To whom correspondence should be addressed.
  pengy@lzu.edu.cn
‡To whom correspondence should be addressed.
  hongxin.yang@nimte.ac.cn

§To whom correspondence should be addressed.
jiang_lab@tsinghua.edu.cn

[1] M. Bode, M. Heide, K. von Bergmann, P. Ferriani, S. Heinze, G. Bihlmayer, A. Kubetzka, O. Pietzsch, S. Blugel, and R. Wiesendanger, Chiral magnetic order at surfaces driven by inversion asymmetry, Nature (London) **447**, 190 (2007).

[2] F. Hellman et al., Interface-induced phenomena in magnetism, Rev. Mod. Phys. **89**, 025006 (2017).

[3] L. Shekhtman, O. Entin-Wohlman, and A. Aharony, Moriya's Anisotropic Superexchange Interaction, Frustration, and Dzyaloshinsky's Weak Ferromagnetism, Phys. Rev. Lett. **69**, 836 (1992).

[4] A. Crépieux and C. Lacroix, Dzyaloshinsky-Moriya interactions induced by symmetry breaking at a surface, J. Magn. Magn. Mater. **182**, 341 (1998).

[5] M. Heide, G. Bihlmayer, and S. Blügel, Dzyaloshinskii-Moriya interaction accounting for the orientation of magnetic domains in ultrathin films: Fe/W(110), Phys. Rev. B **78**, 140403(R) (2008).

[6] H. T. Nembach, J. M. Shaw, M. Weiler, E. Jué, and T. J. Silva, Linear relation between Heisenberg exchange and interfacial Dzyaloshinskii-Moriya interaction in metal films, Nat. Phys. **11**, 825 (2015).

[7] S. Emori, U. Bauer, S. M. Ahn, E. Martinez, and G. S. Beach, Current-driven dynamics of chiral ferromagnetic domain walls, Nat. Mater. **12**, 611 (2013).

[8] G. Chen, T. Ma, A. T. N'Diaye, H. Kwon, C. Won, Y. Wu, and A. K. Schmid, Tailoring the chirality of magnetic domain walls by interface engineering, Nat. Commun. **4**, 1 (2013).

[9] K. S. Ryu, L. Thomas, S. H. Yang, and S. Parkin, Chiral spin torque at magnetic domain walls, Nat. Nanotechnol. **8**, 527 (2013).

[10] O. Boulle, S. Rohart, L. D. Buda-Prejbeanu, E. Jue, I. M. Miron, S. Pizzini, J. Vogel, G. Gaudin, and A. Thiaville, Domain Wall Tilting in the Presence of the Dzyaloshinskii-Moriya Interaction in Out-of-Plane Magnetized Magnetic Nanotracks, Phys. Rev. Lett. **111**, 217203 (2013).

[11] G. Chen, J. Zhu, A. Quesada, J. Li, A. T. N'Diaye, Y. Huo, T. P. Ma, Y. Chen, H. Y. Kwon, C. Won, Z. Q. Qiu, A. K. Schmid, and Y. Z. Wu, Novel Chiral Magnetic Domain Wall Structure in Fe/Ni/Cu(001) Films, Phys. Rev. Lett. **110**, 177204 (2013).

[12] A. Fert, V. Cros, and J. Sampaio, Skyrmions on the track, Nat. Nanotechnol. **8**, 152 (2013).

[13] J. Sampaio, V. Cros, S. Rohart, A. Thiaville, and A. Fert, Nucleation, stability and current-induced motion of isolated magnetic skyrmions in nanostructures, Nat. Nanotechnol. **8**, 839 (2013).

[14] W. Jiang, P. Upadhyaya, W. Zhang, G. Yu, M. Benjamin, Jungfleisch, F. Y. Fradin, J. E. Pearson, Y. Tserkovnyak, K. L. Wang, O. Heinonen, S. G. E. t. Velthuis, and A. Hoffmann, Blowing magnetic skyrmion bubbles, Science **349**, 283 (2015).

[15] S. Woo, K. Litzius, B. Kruger, M. Y. Im, L. Caretta, K. Richter, M. Mann, A. Krone, R. M. Reeve, M. Weigand, P. Agrawal, I. Lemesh, M. A. Mawass, P. Fischer, M. Klaui, and G. S. Beach, Observation of room-temperature magnetic skyrmions and their current-driven dynamics in ultrathin metallic ferromagnets, Nat. Mater. **15**, 501 (2016).

[16] W. Jiang, G. Chen, K. Liu, J. Zang, S. G. E. te Velthuis, and A. Hoffmann, Skyrmions in magnetic multilayers, Phys. Rep. **704**, 1 (2017).

[17] F. Buttner, I. Lemesh, M. Schneider, B. Pfau, C. M. Gunther, P. Hessing, J. Geilhufe, L. Caretta, D. Engel, B. Kruger, J. Viefhaus, S. Eisebitt, and G. S. D. Beach, Field-free deterministic ultrafast creation of magnetic skyrmions by spin-orbit torques, Nat. Nanotechnol. **12**, 1040 (2017).

[18] S. Huang, C. Zhou, G. Chen, H. Shen, A. K. Schmid, K. Liu, and Y. Wu, Stabilization and current-induced motion of antiskyrmion in the presence of anisotropic Dzyaloshinskii-Moriya interaction, Phys. Rev. B **96**, 144412 (2017).

[19] A. Fernandez-Pacheco, E. Vedmedenko, F. Ummelen, R. Mansell, D. Petit, and R. P. Cowburn, Symmetry-breaking interlayer Dzyaloshinskii-Moriya interactions in synthetic antiferromagnets, Nat. Mater. **18**, 679 (2019).

[20] D. H. Kim, M. Haruta, H. W. Ko, G. Go, H. J. Park, T. Nishimura, D. Y. Kim, T. Okuno, Y. Hirata, Y. Futakawa, H. Yoshikawa, W. Ham, S. Kim, H. Kurata, A. Tsukamoto, Y. Shiota, T. Moriyama, S. B. Choe, K. J. Lee, and T. Ono, Bulk Dzyaloshinskii-Moriya interaction in amorphous ferrimagnetic alloys, Nat. Mater. **18**, 685 (2019).

[21] E. Y. Vedmedenko, P. Riego, J. A. Arregi, and A. Berger, Interlayer Dzyaloshinskii-Moriya Interactions, Phys. Rev. Lett. **122**, 257202 (2019).

[22] O. G. Udalov and I. S. Beloborodov, Strain-dependent Dzyaloshinskii-Moriya interaction in a ferromagnet/heavy-metal bilayer, Phys. Rev. B **102**, 134422 (2020).

[23] L. Liu, J. Yu, R. González-Hernández, C. Li, J. Deng, W. Lin, C. Zhou, T. Zhou, J. Zhou, H. Wang, R. Guo, H. Y. Yoong, G. M. Chow, X. Han, B. Dupé, J. Železný, J. Sinova, and J. Chen, Electrical switching of perpendicular magnetization in a single ferromagnetic layer, Phys. Rev. B **101**, 220402(R) (2020).

[24] D. S. Han, K. Lee, J. P. Hanke, Y. Mokrousov, K. W. Kim, W. Yoo, Y. L. W. van Hees, T. W. Kim, R. Lavrijsen, C. Y. You, H. J. M. Swagten, M. H. Jung, and M. Klaui, Long-range chiral exchange interaction in synthetic antiferromagnets, Nat. Mater. **18**, 703 (2019).

[25] M. Tang, K. Shen, S. Xu, H. Yang, S. Hu, W. Lu, C. Li, M. Li, Z. Yuan, S. J. Pennycook, K. Xia, A. Manchon, S. Zhou, and X. Qiu, Bulk spin torque-driven perpendicular magnetization switching in L10 FePt single layer, Adv. Mater. **32**, 2002607 (2020).

[26] L. Zhu, X. S. Zhang, D. A. Muller, D. C. Ralph, and R. A. Buhrman, Observation of strong bulk damping-like spin-orbit torque in chemically disordered ferromagnetic single layers, Adv. Funct. Mater. **30**, 2005201 (2020).

[27] L. Zhu, D. C. Ralph, and R. A. Buhrman, Unveiling the mechanism of bulk spin-orbit torques within chemically disordered FexPt1–x single layers, Adv. Funct. Mater. **31**, 2103898 (2021).

[28] A. Fert and P. M. Levy, Role of Anisotropic Exchange Interactions in Determining the Properties of Spin-Glasses, Phys. Rev. Lett. **44**, 1538 (1980).

[29] P. M. Levy and A. Fert, Anisotropy induced by nonmagnetic impurities in CuMn spin-glass alloys, Phys. Rev. B **23**, 4667 (1981).

[30] P. M. Levy, C. Morgan-Pond, and A. Fert, Origin of anisotropy in transition metal spin glass alloys (invited), J. Appl. Phys. **53**, 2168 (1982).

[31] See Supplemental Material at http://link.aps.org/supplemental/10.1103/PhysRevLett.128.167202 for method for first-principles calculations, a list of samples in the main text, the magnetic hysteresis (M-H) loops for the films with magnetization gradient, the composition and magnetic depth profiles, the composition profiles examined by HAADF-STEM and EDS, and the distinction between the interfacial DMI and gradient-induced DMI, which includes Refs. [32–43].

[32] G. Kresse and J. Hafner, *Ab initio* molecular dynamics for liquid metals, Phys. Rev. B **47**, 558(R) (1993).

[33] G. Kresse and J. Furthmüller, Efficient iterative schemes for *ab initio* total-energy calculations using a plane-wave basis set, Phys. Rev. B **54**, 11169 (1996).

[34] G. Kresse and J. Furthmüller, Efficiency of *ab initio* total energy calculations for metals and semiconductors using a plane-wave basis set, Comput. Mater. Sci. **6**, 15 (1996).

[35] H. Yang, G. Chen, A. A. C. Cotta, A. T. N'Diaye, S. A. Nikolaev, E. A. Soares, W. A. A. Macedo, K. Liu, A. K. Schmid, A. Fert, and M. Chshiev, Significant Dzyaloshinskii-Moriya interaction at graphene-ferromagnet interfaces due to the Rashba effect, Nat. Mater. **17**, 605 (2018).

[36] M. Heide, G. Bihlmayer, and S. Blügel, Describing Dzyaloshinskii–Moriya spirals from first principles, Physica (Amsterdam) **B404**, 2678 (2009).

[37] J. Liang, Q. Cui, and H. Yang, Electrically switchable Rashba-type Dzyaloshinskii-Moriya interaction and skyrmion in two-dimensional magnetoelectric multiferroics, Phys. Rev. B **102**, 220409(R) (2020).

[38] Y. Wang and J. P. Perdew, Correlation hole of the spin-polarized electron gas, with exact small-wave-vector and high-density scaling, Phys. Rev. B **44**, 13298 (1991).

[39] G. Kresse and D. Joubert, From ultrasoft pseudopotentials to the projector augmented-wave method, Phys. Rev. B **59**, 1758 (1999).

[40] H. Yang, A. Thiaville, S. Rohart, A. Fert, and M. Chshiev, Anatomy of Dzyaloshinskii-Moriya Interaction at Co/Pt Interfaces, Phys. Rev. Lett. **115**, 267210 (2015).

[41] H. Bai, X. Z. Zhan, G. Li, J. Su, Z. Z. Zhu, Y. Zhang, T. Zhu, and J. W. Cai, Characterization of YIG thin films and vacuum annealing effect by polarized neutron reflectometry and magnetotransport measurements, Appl. Phys. Lett. **115**, 182401 (2019).

[42] Z. C. Zheng, Q. X. Guo, D. Jo, D. Go, L. H. Wang, H. C. Chen, W. Yin, X. M. Wang, G. H. Yu, W. He, H. W. Lee, J. Teng, and T. Zhu, Magnetization switching driven by current-induced torque from weakly spin-orbit coupled Zr, Phys. Rev. Research **2**, 013127 (2020).

[43] J. F. K. Cooper, C. J. Kinane, S. Langridge, M. Ali, B. J. Hickey, T. Niizeki, K. Uchida, E. Saitoh, H. Ambaye, and A. Glavic, Unexpected structural and magnetic depth dependence of YIG thin films, Phys. Rev. B **96**, 104404 (2017).

[44] D. Cortés-Ortuño and P. Landeros, Influence of the Dzyaloshinskii-Moriya interaction on the spin-wave spectra of thin films, J. Phys. Condens. Matter **25**, 156001 (2013).

[45] M. Belmeguenai, J.-P. Adam, Y. Roussigné, S. Eimer, T. Devolder, J.-V. Kim, S. M. Cherif, A. Stashkevich, and A. Thiaville, Interfacial Dzyaloshinskii-Moriya interaction in perpendicularly magnetized Pt/Co/AlOx ultrathin films measured by Brillouin light spectroscopy, Phys. Rev. B **91**, 180405(R) (2015).

[46] K. Di, V. L. Zhang, H. S. Lim, S. C. Ng, M. H. Kuok, X. Qiu, and H. Yang, Asymmetric spin-wave dispersion due to Dzyaloshinskii-Moriya interaction in an ultrathin Pt/CoFeB film, Appl. Phys. Lett. **106**, 052403 (2015).

[47] X. Ma, G. Yu, X. Li, T. Wang, D. Wu, K. S. Olsson, Z. Chu, K. An, J. Q. Xiao, K. L. Wang, and X. Li, Interfacial control of Dzyaloshinskii-Moriya interaction in heavy metal/ferromagnetic metal thin film heterostructures, Phys. Rev. B **94**, 180408(R) (2016).

[48] K. Di, V. L. Zhang, H. S. Lim, S. C. Ng, M. H. Kuok, J. Yu, J. Yoon, X. Qiu, and H. Yang, Direct Observation of the Dzyaloshinskii-Moriya Interaction in a Pt/Co/Ni Film, Phys. Rev. Lett. **114**, 047201 (2015).

[49] J.-H. Moon, S.-M. Seo, K.-J. Lee, K.-W. Kim, J. Ryu, H.-W. Lee, R. D. McMichael, and M. D. Stiles, Spin-wave propagation in the presence of interfacial Dzyaloshinskii-Moriya interaction, Phys. Rev. B **88**, 184404 (2013).

[50] R. A. Gallardo, P. Alvarado-Seguel, T. Schneider, C. Gonzalez-Fuentes, A. Roldán-Molina, K. Lenz, J. Lindner, and P. Landeros, Spin-wave non-reciprocity in magnetization-graded ferromagnetic films, New J. Phys. **21**, 033026 (2019).

[51] R. A. Gallardo, T. Schneider, A. K. Chaurasiya, A. Oelschlägel, S. S. P. K. Arekapudi, A. Roldán-Molina, R. Hübner, K. Lenz, A. Barman, J. Fassbender, J. Lindner, O. Hellwig, and P. Landeros, Reconfigurable Spin-Wave Nonreciprocity Induced by Dipolar Interaction in a Coupled Ferromagnetic Bilayer, Phys. Rev. Applied **12**, 034012 (2019).

[52] O. Gladii, M. Haidar, Y. Henry, M. Kostylev, and M. Bailleul, Frequency nonreciprocity of surface spin wave in permalloy thin films, Phys. Rev. B **93**, 054430 (2016).

[53] A. Fernández-Pacheco, R. Streubel, O. Fruchart, R. Hertel, P. Fischer, and R. P. Cowburn, Three-dimensional nanomagnetism, Nat. Commun. **8**, 15756 (2017).